**PAPER** • **OPEN ACCESS**

# A piezoelectric coded-excitation scanning acoustic transducer for Lamb wave inspections



OPEN ACCESS
IOP Publishing
Smart Materials and Structures
Smart Mater. Struct. **34** (2025) 025021 (18pp)
https://doi.org/10.1088/1361-665X/ada07b

# A piezoelectric coded-excitation scanning acoustic transducer for Lamb wave inspections

**Marco Dibiase, Masoud Mohammadgholiha and Luca De Marchi***

Department of Electrical, Electronic, and Information Engineering 'Guglielmo Marconi', University of Bologna, Bologna 40136, Italy

E-mail: l.demarchi@unibo.it

Received 31 July 2024, revised 11 November 2024
Accepted for publication 17 December 2024
Published 15 January 2025

**Abstract**

Several techniques for Guided Wave (GW) inspections have already been developed. Most of them rely on extensive sensor deployment and damage localization algorithms characterized by significant computational costs. However, there is a growing demand for simpler, more autonomous, and more affordable systems across various fields. In particular, the implementation of wireless, battery-powered systems with a reduced number of sensor nodes and simpler processing would greatly facilitate the transition of this inspection technology on the field. Following this direction, this work presents the design of a novel piezoelectric transducer composed of four different patches, i.e. with only four input/output channels, to scan a given area. The peculiar piezo-load distributions allow the association of different spectral binary sequences for each 6° discrete angular step. By evaluating the distance-of-flights (DoFs) of detected peaks, the range coordinates for multiple defects are identified. Meanwhile, the angular information is extracted by demodulating binary sequences of peaks with comparable DoFs across several frequency bands. Since the transducer is designed as an encoder, it is referred to as coded-excitation scanning acoustic transducer (CESAT). More specifically, the Gray code is used to generate spectral patterns to reduce the uncertainty between two adjacent angular steps. A new quantization procedure for the optimal generation of the piezo distributions is also proposed. Ad hoc signal processing algorithms, suitable for embedded applications, were developed to extract multi-target range and angle information. The processing is based on the frequency decomposition of the recorded signal using an FIR filter bank and on dispersion compensation procedures for pulse *'re-compression'*. The transducer encoder behavior is validated through a finite element analysis. Finally, numerical simulations were performed to assess the effectiveness of the CESAT and associated signal processing in multi-defect detection and localization tasks.

Keywords: coded-excitation scanning acoustic transducer, guided waves, structural health monitoring, Green's functions, finite element simulations, piezoelectric

* Author to whom any correspondence should be addressed.

## 1. Introduction

In the last decades, the field of structural health monitoring (SHM) [1–3] has been increasingly investigated thanks to its potential to reduce maintenance costs and enhance the safety of monitored systems, especially those operating beyond their design life [4]. Among the active monitoring systems capable of performing on-demand inspections and detecting damage, those based on Guided Waves (GWs) [2], such as Lamb Waves [5, 6], are of particular interest. Lamb waves are elastic waves that propagate through thin-wall structures. Thanks to acoustic confinement in these structures, they can travel long distances with little attenuation, making them highly attractive for structural inspections [7]. Piezoelectric transducers [8], bonded to the monitored structure, are widely used to excite ultrasound waves and detect potential echoes caused by defects (*pulse-echo* method) [9]. Alternatively, a secondary transducer can pick up the excited waves (*pitch-catch* method). The direction-of-arrival (DoA) of GWs generated by scattered damage in the material, as well as wave dispersion and attenuation, can be extracted for multi-defect localization.

A considerable number of GW structural inspection techniques have already been developed. Among these, solutions relying on *Interdigital Transducers* [10] and *phased arrays* [11] have been widely tested and employed. *Interdigital Transducers* operate at a fixed frequency, determined by the spacing between the multiple piezoelectric elements. Capineri and Bulletti [12] demonstrated how the mainlobe width of interdigital transducers could be controlled by altering the angle of the electrodes that form the transducer. Crack detection capability was experimentally confirmed in metallic [13] and composite [14] plates using both the $A_0$ mode at lower frequencies and the $S_0$ mode, with wavelengths sufficiently small for effective crack detection. Nevertheless, the scanning capability of interdigital transducers is limited by their fixed directionality. In order to achieve mobile detection directionality, *phased arrays*, well-known and employed in RADAR and SONAR applications, can be used. Beam steering is realized by creating constructive and destructive interference among multiple emitting and receiving elements. This is done by setting the appropriate phases for these elements to transmit focused waves. This process is commonly called *beamforming* or *delay-and-sum* [15].

In the context of GW propagation, the dispersive nature of wave propagating through the medium has to be considered when the beamforming technique is performed [16–18]. It is important to note that reducing the mainlobe beamwidth with phased arrays generally needs a large number of sensors [19], leading to extensive signal processing. Conversely, certain application fields, such as aerospace and aeronautical, require battery-powered systems with low computational cost and a reduced number of sensors to save on weight and cabling [20]. As a result, the phased array solution is often unsuitable for these applications. Therefore, there is a need to develop a novel inspection system capable of performing beam steering without these constraints.

As an alternative to phased array systems, meta-transducers [21, 22] with inherent beamsteering capability can be fruitfully utilized. In particular, Senesi and Ruzzene [23] derived a frequency response of an arbitrary shape piezo-transducer model in the presence of an incoming Lamb wave, which relates the piezo-load distribution to the transducer directivity. By exploiting such a model, they designed a single transducer able to scan the entire 2D monitored area. Its Directivity function was designed so that the scanning direction was controlled by the dominant frequency of the actuated signal. Therefore, It was called frequency steerable acoustic transducer (FSAT). During the last decade, the FSAT has been increasingly investigated, particularly for the following aspects (see [24] for details):

(i) trade-off between angular and radial resolutions;
(ii) optimization of the shape;
(iii) unidirectionality;

The first point, in particular, is related to the fact that the angular resolution of FSATs increases when the actuated pulse is narrowband; however, a narrowband pulse implies a low temporal resolution. In this work, a different design criterion is considered to derive a novel beam steering strategy that is based on a different association between the steering direction and the spectral content of the actuated pulse. More specifically, the transducer is designed following the operating principles of an encoder: a different binary spectral configuration is associated with each discrete angular step, namely an *equivalent mainlobe*. Since the angular coordinates are extracted by demodulating a binary sequence, this transducer is referred to as coded-excitation scanning acoustic transducer (CESAT). The multi-defects range and angle coordinates retrieval are obtained, respectively, by estimating the distances of flight (DoFs) of the detected peaks and demodulating binary sequences of peaks with approximately equal DoFs at various frequency bands. Thanks to the new design criterion, the trade-off between angle and range resolution (point (i)) is significantly less stringent, as detailed in the following. An (equivalent) mainlobe aperture of approximately 6° is achieved without decreasing the range resolution.

Regarding point (ii), it can be generally observed that the transducer shaping is based on the definition of an ideal target function (referred to as *shape function*) describing the piezo-load distribution. Such function is continuously modulated in its values. In contrast, to simplify the practical realization of the transducers shape function must have values set to either 1 or 0.

To cope with this problem, a new quantization procedure based on abrupt threshold values is proposed in this work, and optimized to achieve the desired *Directivity* wavevector-**k**-function. Two different patches are required for the positive and negative values of the shape function.

To tackle point (iii), i.e. to realize unidirectional devices, this work relies on the solutions firstly proposed in [25, 26] which are based on a double-phase quantization method,

which results in the generation of four distinct patches. A formal mathematical explanation/procedure of the signal phase shifts to be applied to the signals actuating the four patches was provided in [24], and it is employed in the present work.

Finally this work introduces a signal processing algorithm specifically dedicated to the transducer characteristics and suitable for embedding in micro-controller units. The algorithm enables multi-defect detection and localization and is based on the deployment of five linear-phase FIR filters for spectral decomposition, dispersion compensation procedures [27] for wave-pulse *'re-compression'* and cross-correlation (CC) products [28].

The spectral encoder behavior of the CESAT is validated through numerical simulations, considering a plate with three reflectors and noisy measurements, and demonstrating the localization accuracy of the proposed device.

## 2. System model

To design an ultrasonic transducer for SHM via GWs, the piezo-load response model in sensing mode, proposed by Senesi and Ruzzene [23] is considered in this work. Let us consider a GW mode impinging on the piezo-patch in the direction $\mathbf{k}$, with typically a non-linear characteristic of frequency $\mathbf{k}(f)$, as illustrated in figure 1. Its surface displacement can generally be expressed as:

$$\mathbf{u}(\mathbf{x},f) = \mathbf{U}(f)\,\mathrm{e}^{-j\mathbf{k}(f)\cdot\mathbf{x}} \tag{1}$$

where the $\mathbf{x} = (x,y)$ coordinates lie in the plane-plate, $\mathbf{U}(f)$ denotes the amplitude and polarization of the wave at frequency $f$, and $\mathbf{k}(f) = k(f)\mathbf{i'}_1 = k(f)(\cos\theta\mathbf{i}_1 + \sin\theta\mathbf{i}_2)$ is the considered wave vector, propagating in the $\mathbf{i'}_1$ plane-direction (with $k(f) = |\mathbf{k}(f)|$ and $[\mathbf{i}_1,\mathbf{i}_2]$ the plane reference system), i.e. at an angle $\theta$.

Let us suppose that the piezo-transducer geometry is described by the shape function $\phi_P(\mathbf{x})$ defined as:

$$\phi_{\mathrm{P}}(\mathbf{x}) = \begin{cases} 1, & \text{if } \mathbf{x} \in \Omega_{\mathrm{P}} \\ 0, & \text{if } \mathbf{x} \in \Omega - \Omega_{\mathrm{P}}. \end{cases} \tag{2}$$

where $\Omega_{\mathrm{P}}$ is the piezo-patch area (not necessarily compact) and $\Omega$ is the entire plate domain. The following assumptions are made:

- the piezo-polarization is 'through-the-thickness.'
- the sensor is assumed in a state of plain strain.
- the considered wave is characterized by an in-plane displacement such that $\mathbf{u}(\mathbf{x},f)\cdot\mathbf{i'}_2 = 0$

The frequency response of the piezo-load is given by [23]:

$$V_{\mathrm{P}}(f,\theta) = jU(f)\,k(f)\,H(\theta)\,D(k(f),\theta) \tag{3}$$

where $H(\theta)$ is related only to the piezo-material properties and involves directional components only if the patch has non-isotropic properties. Instead, the function $D(k(f),\theta) = D(\mathbf{k}(f))$ is given by:

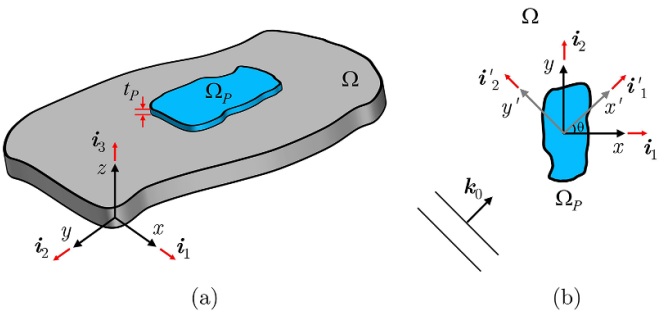


**Figure 1.** Arbitrary shaped transducer model: (a) a thin plate with a bonded, arbitrarily shaped piezoelectric sensor; (b) interaction of the sensor with a plane wave propagating at an angle $\theta$ on the $\mathbf{x}$-plane of the structure.

$$D(\mathbf{k}(f)) = \int_{-\infty}^{\infty}\int_{-\infty}^{\infty} \mathrm{e}^{-j\mathbf{k}(f)\cdot\mathbf{x}}\phi_{\mathrm{P}}(\mathbf{x})\,\mathrm{d}\mathbf{x} \tag{4}$$

This function determines the directional properties of the piezo-distribution $\phi_{\mathrm{P}}(\mathbf{x})$. Therefore, it is referred to as *Directivity function*, and it can be identified as the 2D Fourier Transform (FT) of the shape function. As a consequence, once the desired directivity properties are set, the piezoelectric load distribution can be computed by taking the Inverse FT (IFT) as follows:

$$\phi_P(\mathbf{x}) = F_{2D}^{-1}\{D(\mathbf{k}(f))\} \tag{5}$$

The model in equation (3) is computed assuming that equation (1) represents the displacement under the piezo-area.

To consider the effect of GW dispersion originating at a distance $R$ from the centroid of the distribution $\phi_{\mathrm{P}}(\mathbf{x})$, the surface displacement in equation (1) can be reformulated for the point where the waves are emitted as:

$$\mathbf{u}(\mathbf{x},f) \approx \mathbf{U}(f)\,\mathrm{e}^{-j\mathbf{k}(f)\cdot\left(\mathbf{x}+R\mathbf{i'}_1\right)}. \tag{6}$$

As a consequence, equation (3) for a piezo-load in sensing mode can be restated as:

$$V_{\mathrm{P}}(f,\theta) = jU(f)\,k(f)\,H(\theta)\,D(k(f),\theta)\,\mathrm{e}^{-jk(f)R}. \tag{7}$$

Note that when GWs are generated at a distance $R$ from a piezo sensor in multiple close directions, the previous model is still applicable in the case of nearly planar wavefronts, specifically when:

$$R \gg W \tag{8}$$

where $W = \max|\mathbf{w}_{ij}|$, and $\mathbf{w}_{ij}$ is the set of vectors connecting all possible pairs of points $P_i, P_j$ that belongs to the area of the transducer. Furthermore, for isotropic structures, a propagation attenuation factor proportional to $1/\sqrt{R}$ has to be introduced (according to the energy conservation principle).

Let us observe that in GW sensing mode, the sensor's geometry, through its directivity function, acts as a filter that attenuates or amplifies incoming focused plane waves in any form of equation (6) depending on their directions (i.e. the angle $\theta$) and spectrum. Due to the dual nature of the constitutive equations of a piezoelectric sensor (inverse and direct effect) [29], which establishes the principles of 'acoustic reciprocity,' applying a certain voltage $V(f)$ to the transducer generates focused plane waves with a spectrum $U(f)$. This spectrum is proportional to $V(f)D^*(f,\theta)$, where $D$ is defined in equation (4), and these waves are transmitted in the directions specified by $\theta$. The transducer behavior in active mode will be detailed in section 5.

Note that in the far-field zone, even during the wave generation, a potential wave reflector would be approximately irradiated by multiple focused waves with a negligible angular variation of the wavenumber $k$, effectivity in a single direction. Similarly, the radiating transducer will be illuminated by a single focused plane echo wave.

It is important to note that the described model in equation (7) can be generalized to include displacement with both in-plane and out-of-plane components, while preserving the form of directivity function in equation (4).

As a final note, it is noteworthy to observe that the GW Directivity function provides an amplification factor specific to the transducer, regardless of the amplitude of the excitation signal $S(f)$. Therefore, the term $|D(k(f),\theta)|^2$ affects the *radiation intensity* of the transducer, i.e. the transmitted power per unit angle $\theta$ and wavenumber $k(f)$:

$$|D(k(f),\theta)|^2 \propto \frac{\mathrm{d}P_\mathrm{T}}{\mathrm{d}\theta \mathrm{d}k}. \tag{9}$$

As a result, the directivity function also affects the transducer's maximum range.

## 3. CESAT

Based on the model in equation (5), the piezoelectric load geometric distribution can be defined to achieve the desired directive properties. In previous works, this possibility was exploited for the design of both passive directive sensors [25] and active monitoring systems [30].

In this work, a novel design paradigm is introduced to improve defect detection and localization performance. The aim is to obtain a directivity function that allows for different spectral configurations to be excited in different directions. More specifically, as discussed in section 1, the transducer is designed according to the operating principles of an *encoder*: the angular range of 180° is discretized, and for each discrete angular step, a distinct spectral binary $k$-Bin sequence is considered. Therefore, it is called CESAT. Thanks to the new design criterion, the accuracy of locating a single reflector/damage can be significantly improved.

Considering the encoder concept, the directivity function in the $\mathbf{k} = (k_1, k_2)$ domain, has to be defined to satisfy project specifications and maximize target localization performance.

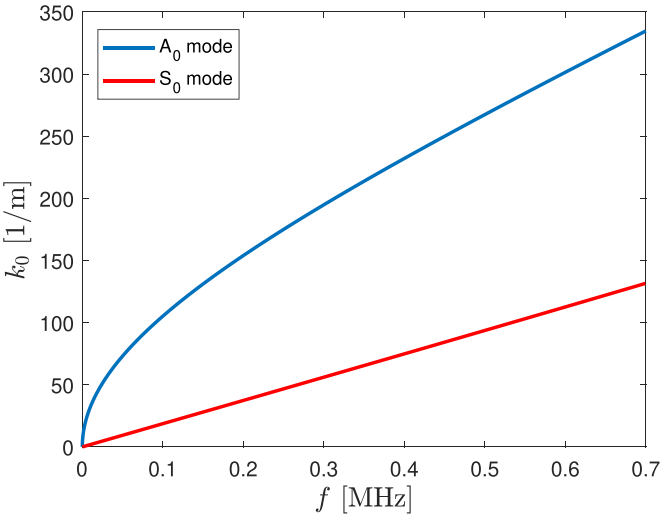


**Figure 2.** Wavenumber $k$ as a function of frequency $f$ (Dispersion Curve) for the $A_0$ and $S_0$ modes of Lamb waves propagating in a 1 mm thick aluminum plate.

Then, the spatial distribution of the piezo-material will be computed using an inverse 2D-FT, according to equation (5).

### 3.1. CESAT: directivity synthesis

To define the Directivity function, it is essential to select the number of *'bin'* for each $k$-configuration, whether set to 1 or 0, and the *bin function*, based on the following key elements:

(i) **Minimum detectable defect size and maximum excitable frequency.**
The minimum detectable defect/damage size determines the minimum wave-vector value. For example, a defect size of 0.5 cm implies the actuation of waves characterized by a maximum half-wavelength of 0.5 cm [31] and, consequently the minimum wavenumber $k$ value has to be set to $100\,\mathrm{m}^{-1}$.
Conversely, the maximum wavenumber value is defined by the maximum frequency value that the embedded systems can excite on the driven sensor load. By way of illustration, in this work, we assume that such value is equal to 450 kHz. The monitored structure considered in the numerical validation is a 1 mm thick aluminum plate. Therefore, the maximum $k$ value of 250 $\mathrm{m}^{-1}$ can be determined from the dispersion curve $k(f)$ of the excited Lamb wave mode, i.e. $A_0$ (figure 2).
The minimum frequency value corresponding to the minimum $k$ value is equal to 90 kHz, via the same curve.
To summarize the previous results, the available band (AB) in $k$ and $f$ are given by [100–250]$\mathrm{m}^{-1}$ and [90–450] kHz, respectively.

(ii) **Maximizing defect angle and range estimation bounds.**
In our approach, the available $k$ band-width (ABW) is partitioned into $n_\mathrm{b}$ bins of equal $k$-bandwidth, then $(2^{n_\mathrm{b}} - 1)$ binary configurations can be employed. This implies that the higher the bin number, the higher the angular resolution (i.e. smaller angular step). Conversely, accurate range

estimation requires broadband bins to enhance the estimation accuracy, as established in Radar antenna theory [32]. The limitations induced by the angle-range resolution trade-off were evident for FSATs (see [33] for details). However, for the CESAT typology, this trade-off is less stringent. Indeed, the FSAT is designed such that the angle and range resolution are inversely proportional and linearly related to the bin bandwidth, respectively. In contrast, for the CESAT, increasing $n_\mathrm{b}$ to $n_\mathrm{b}+1$ reduces the bin bandwidth by only $-\mathrm{ABW}/\left({n_\mathrm{b}}^2-n_\mathrm{b}\right)$. Meantime, the angular step decreases significantly to $1/\left(2^{n_\mathrm{b}+1}-1\right)$. This proves that the proposed CESAT offers a significant advantage in defect localization accuracy compared to the previous beam-steering transducer generations.

In this work, $n_\mathrm{b}$ was set equal to 5, and equal $k$-bandwidth bins were designed. Given $\mathrm{ABW}=150\ \mathrm{m}^{-1}$, the resulting bandwidth per bin is $30\ \mathrm{m}^{-1}$. The central wave numbers $k_{\mathrm{c}-i}$ for these five bin bands are given by the vector:

$$\mathrm{K_c}=(115,145,175,205,235)\ \mathrm{m}^{-1} \tag{10}$$

Regarding the binary sequences, $N_\mathrm{bs}=2^{n_\mathrm{b}}-1=31$ configurations are available. Considering only 30 of these configurations, an angular step of 6° is achieved, which is the nominal angle accuracy.

Finally, the *bin function* in the wave-vector $\mathbf{k}$ has to be selected to maximize range estimation accuracy when the measurements are affected by noise.

Such accuracy maximization can be based on the assumption that a dispersion compensation procedure is applied to the acquired signal (see section 7.1).

It is also assumed that the excitation signal is band-limited both in $f$ and $k$ through the dispersion curve, and its spectrum $S(f(k))\sqrt{df/dk}$ has a flat-band. As a consequence, the spectrum for each bin is defined solely by the bin directivity function $D(k)$.

Under these circumstances, the Cramér–Rao lower bound (CRLB) of the range (distance) of flight (RoF), namely $\delta R^2$, of the inspection signal $d(r)$, can be derived from the Radar theory [34–36]: in case of white noise, the range estimation bound $\delta R$ is given by:

$$\delta R=\frac{1}{\beta(2E/N_0)^{1/2}} \tag{11}$$

where $E$ is the energy signal, $N_0$ is the power per unit frequency, $E/N_0$ is the signal-to-noise ratio (SNR) in energy, and $\beta$ is defined as:

$$\begin{aligned}\beta^2&=\frac{\int_{-\infty}^{\infty}(2\pi k)^2|D(k)|^2\mathrm{d}k}{\int_{-\infty}^{\infty}|D(k)|^2\mathrm{d}k}\\&=\frac{1}{E}\int_{-\infty}^{\infty}(2\pi k)^2|D(k)|^2\mathrm{d}k\end{aligned} \tag{12}$$

in which, $|D(k)|^2$ is the two-sided energy spectrum. $\beta$ is called *Effective Bandwidth* and is equal to the second moment of the frequency energy distribution of the bin, normalized by its energy.

According to [32], when a stationary continuous band signal is employed, the optimal signal is given by the Gaussian packet which provides the maximum $\beta$ value equal to $2.66B_\mathrm{HP}$, where $B_\mathrm{HP}$ is the half-power bandwidth. This result is justified as the Gaussian signal allows to have a smoother frequency spectrum and, in a dual way, sharper rise and fall time fronts.

As a result, if a flat-band signal is excited (at least for each bin), it can be concluded that the optimal solution is achieved by using a Gaussian function.

Furthermore, observe that the Gaussian $k$-bin has the minimum time–frequency uncertainty product. Therefore, the Gaussian function in the wave-vector domain allows the minimization of the transducer size.

The Directivity function for a 'building Bin' rotated by an angle $\xi$ (counter-clockwise) and translated by $k_\mathrm{c}$ is, consequently, described as follows:

$$D(k(f),\theta)=\exp\left(-\frac{1}{2}\frac{(k-k_\mathrm{c})^2}{\sigma_k^2}\right)\mathrm{rect}\left(\frac{\theta-\xi}{\Delta\theta}\right). \tag{13}$$

The corresponding shape function is given by:

$$\begin{aligned}|f(r,\alpha)|&=\left|\sqrt{2\pi}\sigma_k\Delta\theta\exp\left(-\frac{1}{2}\frac{r^2}{\sigma_r^2}\right)\mathrm{sinc}\left(\Delta\theta(\alpha-\xi)\right)\right|\\&=\left|\sqrt{2\pi}\sigma_k\frac{l_k}{k_\mathrm{c}}\exp\left(-\frac{1}{2}\frac{r^2}{\sigma_r^2}\right)\mathrm{sinc}\left(\frac{l_k}{k_\mathrm{c}}(\alpha-\xi)\right)\right|\end{aligned} \tag{14}$$

where $l_k$ is the wedge arc length for $k=k_\mathrm{c}$, and $\sigma_r^2=1/2\pi\sigma_k^2$.

In light of technological feasibility, particularly related to the realizability of piezo-load distribution via a quantization process, the standard deviation (SD) $\sigma_k$ is set to 6 $\mathrm{m}^{-1}$.

(iii) **Unidirectionality.**
A real shape function $\phi_\mathrm{P}(\mathbf{x})$ is obtained from equation (5) if and only if the designed Directivity function $D(\mathbf{k})$ satisfies the Hermitian ('symmetric') property. In the context of GW sensing via the Piezo-transducer, it means that it is impossible to determine whether a wave is received from angle $\theta$ or $\theta+180°$. In order to avoid such 180° ambiguity, a 'non-symmetric' directivity function has to be designed. Therefore, in the present work, the synthesis of a complex shape function $\phi_\mathrm{P}(\mathbf{x})$ is considered. The excitation signals suitable for such a complex shape function will be discussed in section 6.2.

(iv) **Minimizing the DoA uncertainty when a defect/damage is placed between two different discrete angular steps.**
To minimize the uncertainty in DoA estimation when a defect or damage is positioned between two distinct angular increments, careful selection of the binary configuration sequence is crucial. The use of *Gray Code* [37] is particularly significant in applications involving the conversion between analog and digital information. For instance, in scenarios where two adjacent angular steps are characterized by binary configurations such as 00101 and

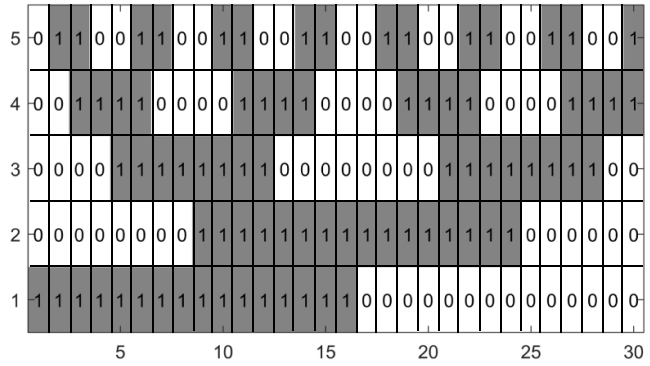

**Figure 3.** Gray code scheme generated with 5 bit (only 30 binary sequences on 31).

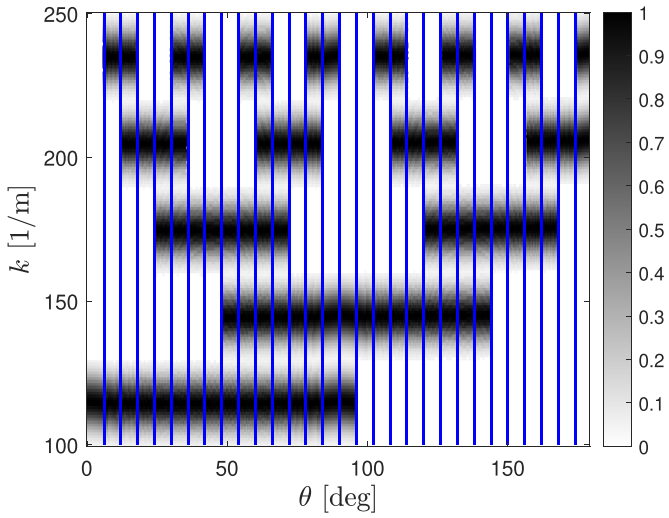


**Figure 4.** Designed directivity function in $k,\theta$-space.

11111, significant inaccuracies can arise at the boundaries between angular sectors due to a smooth transition. The key feature of Gray code is that only one binary digit changes between two adjacent sequences.
Employing the Gray code ensures that the estimation of the angular step between adjacent steps in both frequency and wavenumber $k$ may differ from the nominal value by only one adjacent step. This occurs only when a defect is positioned between two angular steps, resulting in an *equivalent mainlobe* that is slightly larger than 6°.

To summarize, following the Gray code bit-vectors scheme (see figure 3), for each 6° angular step, a Gaussian bin function on a 30 $\mathrm{m}^{-1}$ $k$-support is placed if a bit is set to 1, moving along $k$ within the ABW. Figure 4 shows the resulting Directivity function in the $k,\theta$-space. This function is designed in the wave-vector $\mathbf{k}=(k_1,k_2)$ space (figure 5), in order to use equation (5) and compute the piezoelectric load distribution.

## 4. CESAT: piezoelectric load distribution synthesis

The ideal piezoelectric load distribution $\phi_{\mathrm{P}}(\mathbf{x})$ is computed by using equation (5). This yields a complex shape function due

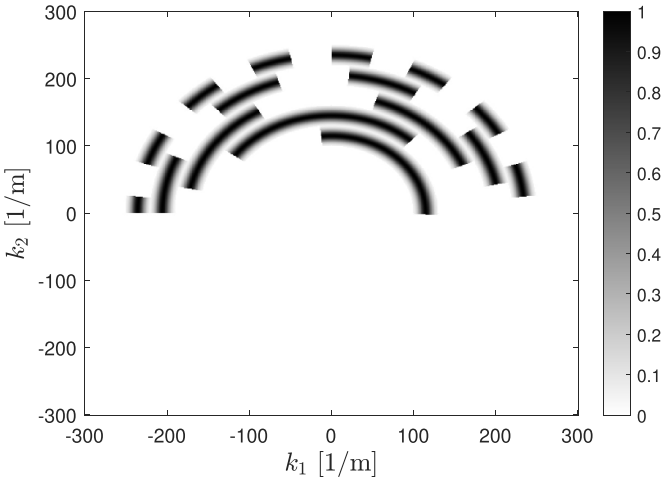


**Figure 5.** Designed Directivity function in the wave-vector $\mathbf{k}=(k_1,k_2)$ space. It can be used to compute the piezo-transducer load distribution via a 2D-IFT (equation (5)).

to the non-Hermitian directivity function shown in figure 5. Its real and imaginary parts are shown in figures 6(a) and (b). Such a shape function, with complex continuously modulated values, must be translated into a piezo-load distribution, whose 2D FT closely approximates the designed directivity function. To this aim, a suitable quantization procedure is required.

### 4.1. Shape function quantization

First, the numerical zero-padding technique is applied to the target Directivity function $D_{\mathrm{T}}(\mathbf{k})$ (figure 5) to generate the ideal shape function $\phi_{\mathrm{P}}(\mathbf{x})$. This technique increases the resolution in the space-domain without reducing the resolution in the $\mathbf{k}$-space. Higher spatial resolution generally allows for better results in approximating the shape function $\phi_{\mathrm{P}}(\mathbf{x})$ and, consequently, its directivity function $D(\mathbf{k})$, regardless of the chosen quantization procedure. Screen printing techniques allow to achieve a spatial resolution of 200 $\mu$m which is the one assumed in this work.

Second, a new optimized $\phi_{\mathrm{P}}(\mathbf{x})$ quantization procedure is applied according to the following steps:

(i) The complex function $\phi_{\mathrm{P}}(\mathbf{x})$ (normalized to the maximum value of $|\phi_{\mathrm{P}}(\mathbf{x})|$ ) is subdivided in two subregions: if $|\mathrm{atan}(\mathrm{Im}(\phi_{\mathrm{P}}(\mathbf{x}))/\mathrm{Re}(\phi_{\mathrm{P}}(\mathbf{x})))| < \pi/4$ or $> 3\pi/4$, $\mathbf{x}$ is assumed to be part of the real region, otherwise $\mathbf{x}$ belongs to the imaginary part. Then, in each region, the complex function undergoes a 3-level quantization so that four different patches are generated.

(ii) More specifically, four different threshold values, $(t_{\mathrm{P1}},t_{\mathrm{P2}},t_{\mathrm{P3}},t_{\mathrm{P4}}) \triangleq \mathbf{T}$ are used respectively to separate in each subregion positive and negative values. The values of the four patches are set to 1 (or $-1$ for negative values) if their magnitude is greater than the threshold value $t_{\mathrm{P}i}$, and 0 otherwise.
The optimal threshold vector $\mathbf{T}_{\mathrm{Opt}}$ is defined as the one which minimizes the mean square error (MSE) between the values of the 2D-FT of the thresholded

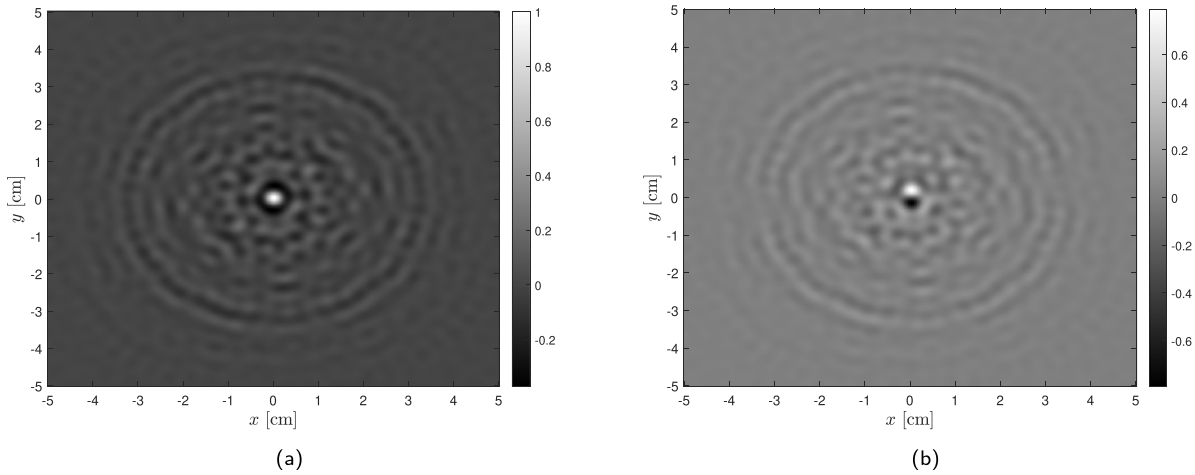


**Figure 6.** (a) Real part of the ideal shape function $\phi_{\mathrm{P}}(\mathbf{x})$; (b) imaginary part of the ideal shape function $\phi_{\mathrm{P}}(\mathbf{x})$.

global function/matrix $\mathrm{FT}_{2\mathrm{D}}\{M_{\mathrm{CESAT}}(\mathbf{T})\}(\mathbf{k}_i)$ and the target directivity function $D_{\mathrm{T}}(\mathbf{k}_i)$. The minimization process exclusively considers the $k$-band of interest, namely [100–250] $\mathrm{m}^{-1}$. Furthermore, a $\lambda$ parameter is used to distinctly control the upper and lower half-planes in the $\mathbf{k}$-plane:

$$\mathbf{T}_{\mathrm{Opt}} \doteq \arg\min \left\{ \begin{array}{l} \lambda \left[ \sum_{i=1}^{M} \left| \mathrm{FT}_{2\mathrm{D}}\{M_{\mathrm{CESAT}}(\mathbf{T})\}(\mathbf{k}_i) - D_{\mathrm{T}}(\mathbf{k}_i) \right|^2 \right]_{k_y<0} \\ +(1-\lambda) \\ \cdot \left[ \sum_{i=1}^{M} \left| \mathrm{FT}_{2\mathrm{D}}\{M_{\mathrm{CESAT}}(\mathbf{T})\}(\mathbf{k}_i) - D_{\mathrm{T}}(\mathbf{k}_i) \right|^2 \right]_{k_y>0} \end{array} \right\}. \tag{15}$$

The $\lambda$ weight parameter is set to 0.35 to optimize the directivity properties in the upper $\mathbf{k}$-half-plane ($k_y > 0$), thereby limiting potential sidelobes in the opposite direction. The optimal threshold values vector was found to be equal to $\mathbf{T}_{\mathrm{Opt}} = (0.065, 0.105, 0.11, 0.03)$.

(iii) To facilitate the practical realization of the transducer, boundary contact lines among different patches are traced and set to 0 to prevent any unwanted short circuits among the four patch segments. (see figure 7). This process resulted in minimal degradation in the directivity function, which remains nearly unchanged despite small variations in patch shapes due to potential manufacturing inaccuracies.

Figure 7 illustrates the piezoelectric load resulting from the previous quantization process. It is composed of four distinct patches. Observe that the last ones correspond to the opposite phases 0 and $\pi$ and $\pi/2$ and $3/2\pi$. This implies that piezopatches related to the real part require just one differential acquisition channel, as do the imaginary ones.

It is worth noting that all areas related to the same patch have to be short-circuited. This can be done directly during the transducer manufacturing process, as experimentally demonstrated in [26].

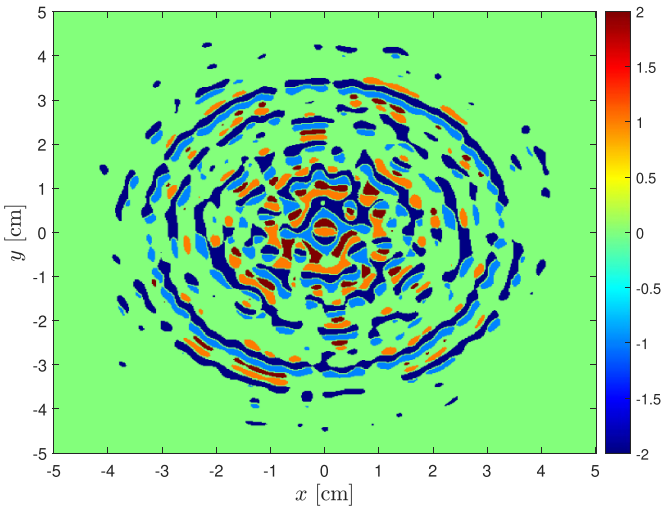


**Figure 7.** Spatial load distribution after the quantization process.

### 4.2. Directivity properties

The achieved directivity function of the CESAT, obtained after the quantization process and computed via equation (4), is illustrated in figure 8. A strong component around the zero-wave-number value is noticeable. This stems from the quantization process, which aims to optimize the directivity function only within the bandwidth of interest, AB = [100–250] $\mathrm{m}^{-1}$. Therefore, the procedure allows the directivity function to deviate from the imposed one outside of AB, as they can be easily filtered out.

Noteworthy, the wave-number range of the Lamb wave S0 mode corresponding to the $f$-AB is [19–84] $\mathrm{m}^{-1}$ (see figure 2). The directivity energy burst around the DC component in figure 8 has a radius of 15 $\mathrm{m}^{-1}$. As a result, the directivity filtering effectively attenuates the S0 component.

The achieved directivity properties can be better represented by considering only the AB in $k-\theta$-space, as shown in figure 9. When compared to the ideal function shown in figure 4(a) certain degradation is visible. This degradation is

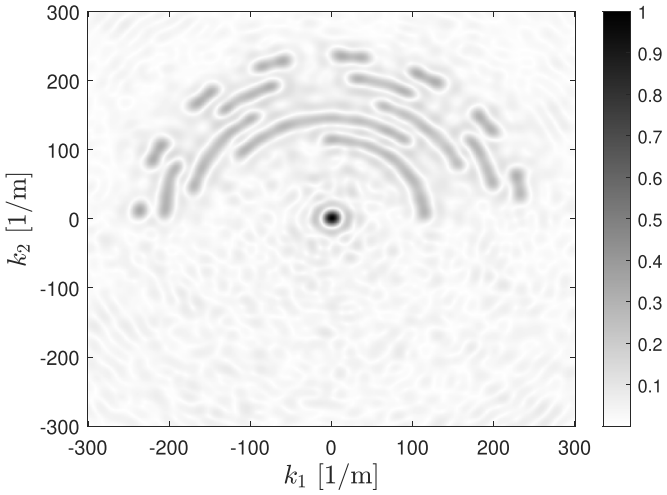


**Figure 8.** Directivity function achieved after the quantization procedure.

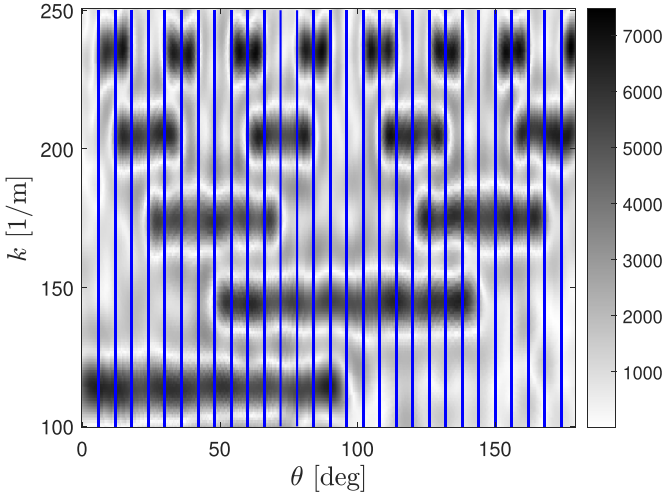


**Figure 9.** Directivity function achieved after the quantization procedure.

attributed to the quantization procedure with abrupt threshold values and, to analyze its impact, it is useful to define the transducer beam-pattern function for the different bands. This function, related to the $i$th wavenumber-band is defined as:

$$d(k-\text{Band}_i.\theta) = \frac{\sum_{k\in k-\text{Band}_i} |D(k,\theta)|}{\max_\theta \left[\sum_{k\in k-\text{Band}_i} |D(k,\theta)|\right]}. \quad (16)$$

It is important to observe that different beampatterns are computed by using equation (16) for different $k$-bands with central wavenumbers given by the values in vector (10), and considering 9 $\text{m}^{-1}$ as bandwidths. This is due to the peculiarity of the implemented Directivity function $D(k,\theta)$, that is characterized by five distinct beampatterns associated to the five different bin location bands.

As observed (see figure 10), the mainlobe level of each beampattern is consistently above 0.68. Meanwhile, the sidelobe level remains below 0.32 value. Higher levels of these sidelobes do not compromise the accurate detection of defects but result in a slightly wider *equivalent mainlobe* for defect angle estimation compared to the nominal value of 6°.

## 5. CESAT numerical validation: actuation mode simulation

To verify the transducer performance, finite element (FE) simulations were conducted using COMSOL Multiphysics® [38]. A three-dimensional FE model was developed, coupling Structural Mechanics and Electrostatics to assess the directional performance of the CESAT in actuation mode. Leveraging the principle of acoustic reciprocity, the transducer operates as an actuator similarly to its sensing mode [26]. In this section, frequency domain simulations were used to evaluate the transducer's beampatterns at different frequencies.

### 5.1. Simulation setup

In this context, a 1 mm thick aluminum plate with dimensions 500 × 500 mm was considered as the propagation medium. As depicted in figure 11, the transducer shape was modeled on a 0.2 mm thick PZT plate with dimensions 80 × 80 mm, which is glued to the aluminum plate using a bonding layer of 30 $\mu$m thickness. The elastic and piezoelectric properties of the aluminum plate, PZT, and the epoxy layer are displayed in Table 1. Perfectly matched layers were implemented at the plate boundaries to minimize wave back-reflection. The bottom surface of the PZT plate was grounded, while an electrical boundary condition was applied to the top surface. Note that loads with specific phase shifts were assigned to patches belonging to different electrode groups. To reduce the computational cost of the model, frequencies ranging from 90 to 270 kHz corresponding to wavenumbers from 100 to 180 $\text{m}^{-1}$ were considered for beampattern validation. As for the meshing, the aluminum and PZT plates were meshed with Free Triangular elements with a size of 0.8 mm, which is $\frac{1}{7}$ of the shortest wavelength achievable by the A0 mode, followed by a swept mesh along the $z$-direction.

### 5.2. Frequency domain simulations

The outcome of the employed frequency domain simulation is presented in terms of the absolute out-of-plane displacement field, to highlight the transducer's directional features. Figure 12 illustrates the displacement wavefield for three wavenumber intervals, namely [111–119] $\text{m}^{-1}$, [141–149] $\text{m}^{-1}$, and [171–179] $\text{m}^{-1}$. As seen, the generated wavefields demonstrate the expected directional behavior of the proposed

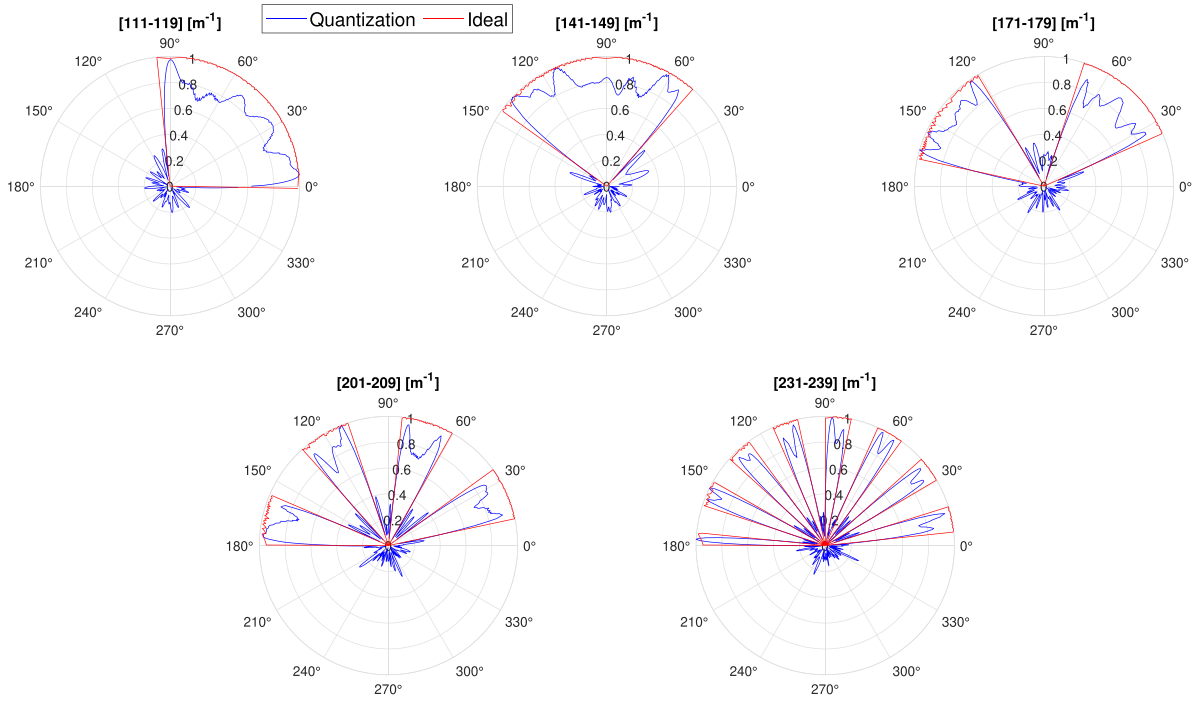


**Figure 10.** Theoretical CESAT beampatterns computed at 5 different $k$-band.

**Table 1.** Elastic and piezoelectric properties of the materials used in the simulation.

| Property | Aluminum | Epoxy Glue | PIC-255 |
|---|---|---|---|
| Density, $\rho$ (kg m$^{-3}$) | 2750 | 1150 | 7800 |
| Elastic modulus (GPa) | 70 | 4.7 | $C_{11} = C_{22} = 132.7$<br>$C_{12} = 86.67$<br>$C_{13} = C_{23} = 85.6$<br>$C_{33} = 119.2$<br>$C_{44} = C_{55} = 21.3$<br>$C_{66} = 22.9$ |
| Poisson ratio | 0.33 | 0.35 | — |
| Piezoelectric constants, $d_{kij}$ (C N$^{-1}$) | — | — | $d_{31} = -187 \times 10^{-12}$<br>$d_{33} = 400 \times 10^{-12}$<br>$d_{15} = 617 \times 10^{-12}$ |
| Electrical permittivity, $\epsilon_{jk}$ | — | — | $\epsilon_{11} = 1852$<br>$\epsilon_{33} = 1751$ |

transducer, highlighting the accuracy of the FE model compared to the analytical results.

$$\begin{matrix} T_1 = (R_1 = 0.25\,\text{m}\ , \theta_1{=}33^\circ) \\ T_2 = (R_2 = 0.45\,\text{m}\ , \theta_2{=}165^\circ) \\ T_3 = (R_3 = 0.65\,\text{m}\ , \theta_3{=}152^\circ) \end{matrix} . \tag{17}$$

## 6. Sensing mode simulation

### 6.1. Time domain simulations

To further validate the CESAT directivity properties, time domain simulations were also carried out, leveraging two different simulation approaches. The first one employs Green's function (GF) formalism [30], to mimic the Lamb wave mode propagation. The second approach uses FE analysis. Simulations were conducted considering three different reflector scenarios in the monitored area (see figure 14):

Given the computational cost associated with simulating the FE full geometry, a subsection of the plate was modeled for each scenario, surrounded by low-reflecting boundary conditions [25, 39]. Due to the reciprocity between the wave excitation and acquisition phases via a piezo-transducer, the latter was simulated by operating the transducer passively. Therefore, the excitation signal was applied at a specific angle and distance from the transducer. The acquired signal was then re-injected at the same angle and distance to simulate the effect of an ideal reflector. This procedure was repeated three times, corresponding to the number of targets.

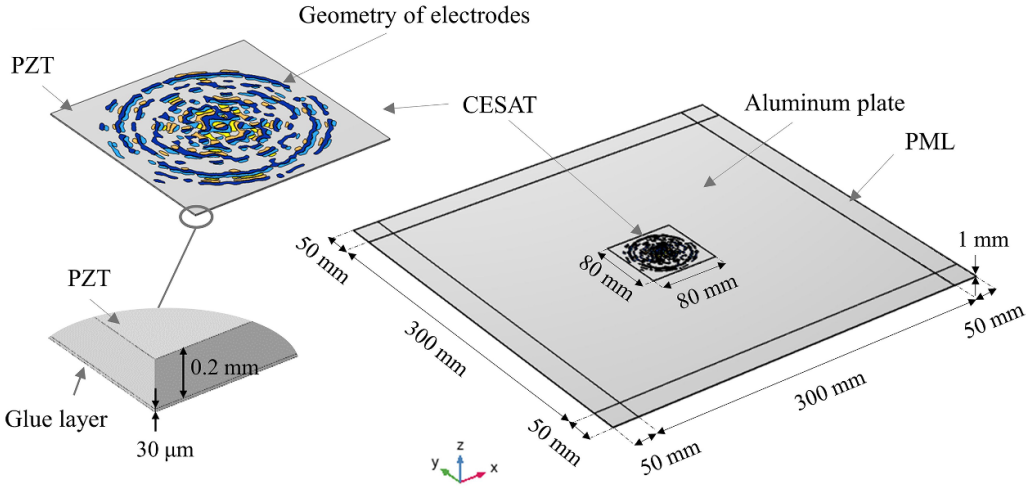


**Figure 11.** 3D geometry of the model.

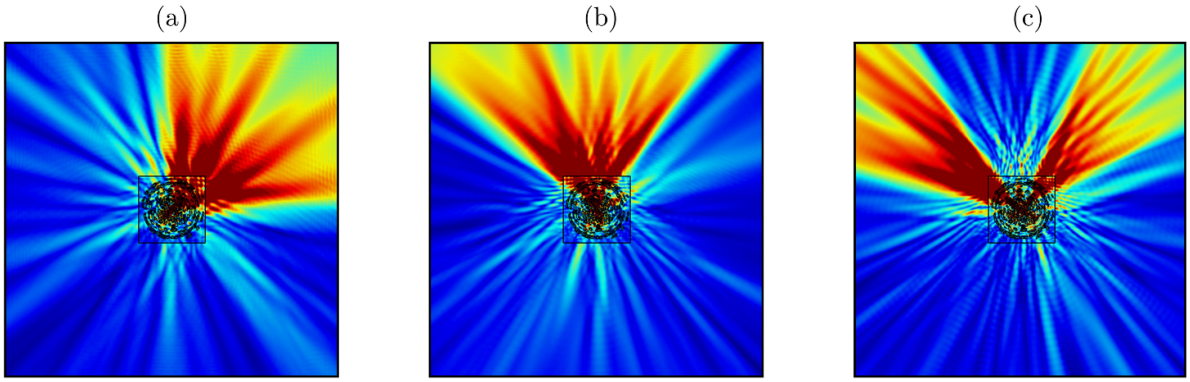


**Figure 12.** Displacement wavefield for three wavenumber intervals: (a) [111–119] $\mathrm{m}^{-1}$; (b) [141–149] $\mathrm{m}^{-1}$; (c) [171–179] $\mathrm{m}^{-1}$.

### 6.2. Actuated signal: overlapped Gaussian pulse (GP) train

According to the procedure derived in [24] via the mathematical model (7), to scan in the $\theta$ direction, the imaginary patch excitation signal must be in quadrature with respect to the real one. To inspect the opposite direction ($\theta$+180°), the imaginary patch excitation signal must be multiplied by $-1$. Therefore, the imaginary signal can be analytically computed as the Hilbert transform (HT) of the real signal (or as -HT to scan the $\theta$+180° direction).

For the CESAT time analysis, an excitation signal suitable for detecting and localizing damage was considered. Indeed, the inspection signal can be selected to enhance radial resolution, noise robustness, and coverage range. At the same time, its excitation has to be compatible with the limited amplification capabilities typical of embedded electronics.

A train of GP, partially overlapped in time, was selected as the excitation signal, due to the benefits for range accuracy highlighted in section (ii). This signal will also be used in the following for 2D damage imaging.

The carrier frequencies of each GP were selected according to the corresponding frequency values of the bin central wavenumbers (10), via the dispersion curve $k(f)$ of the $A_0$ mode of an aluminum plate (figure 2):

$$\mathbf{F}_{\mathrm{c}} = (118, 179, 249, 326, 407)\ \mathrm{kHz}. \tag{18}$$

Each GP was assigned a 23 kHz half-power bandwidth to encompass all the bin $f$-bandwidths, as computed from the dispersion curve $k(f)$ of the $A_0$ Lamb mode. The considered GPs, the excitation signal as their sum, and the associated FFT are illustrated in figure 13.

### 6.3. GF and FE simulation results

The simulation results, related to the three different targets $T_i$, are presented in terms of the transducer's measured (normalized) response and compared with those obtained using the GF method, as displayed in figure 15.

An attenuation term of approximately $1/f^2$ emerged from the FE simulations. This is attributable to the structural damping effects (see [40]), which were not taken into account in the theoretical model (7) or the GF simulations. This attenuation was removed to enable a comparison between the two simulation models. The GF and FE results in terms of the signal amplitude spectra are compared in figure 16, demonstrating excellent agreement.

To provide additional insight into the simulation results, the displacement wavefield generated by the reflector in scenario

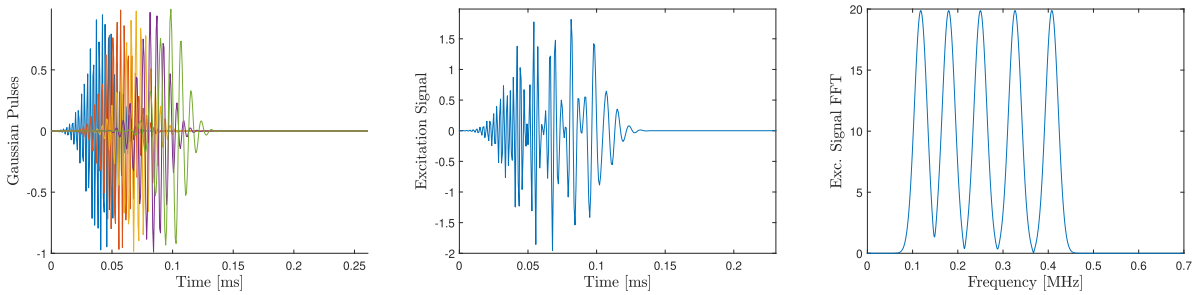


**Figure 13.** (a) Time-Gaussian Pulses with 23 kHz half-power bandwidth; (b) the excitation signal as the sum of the previous GPs; (c) the FFT of the excitation signal (fs = 1.4 MHz).

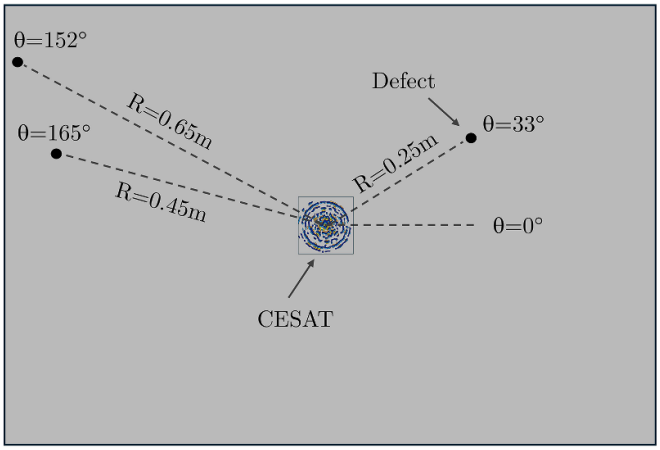


**Figure 14.** Three point targets (defects) considered in the monitored area.

$T_3$ is shown at various time instances in figure 17. This illustrates the propagation of five distinct wave trains with frequencies $f_1$ to $f_5$, traveling from the source location to the transducer. Additionally, time–frequency analysis of the measured signal was performed to reveal the propagation characteristics of each wave packet. The FFT of the signal indicates the intensity of each wave train, highlighting the spatial filtering effect of the transducer to peak only $f_3$ and $f_5$ corresponding to the frequencies of 249 kHz and 407 kHz, as depicted in figure 18.

## 7. Multi-target detection algorithm

The directivity properties of the CESAT allow for the scan of a 2D structure by analyzing just two differential acquired signals from a single device. A potential strategy involves using the pitch-and-catch configuration: a basic omnidirectional transducer generates a broadband signal, while the CESAT captures the GW responses of potential defect reflectors.

Alternatively, the transducer can be used in pulse-echo mode. This latter approach will be considered in the following sections to develop a suitable multi-defect detection and localization algorithm. For 2D localization, both angle and range coordinates have to be estimated from the recorded signal.

As previously detailed (see section 6.2), the train of GPs shown in figure 13 was selected as the inspection signal. This choice was made particularly to suit the CESAT design, ensure compatibility with embedded electronic devices, and optimize multi-target ranging.

### 7.1. Signal processing

According to the transducer's directivity characteristics, angle coordinates are associated with the binary pulse spectral configurations, whereas range coordinates can be evaluated by estimating the DoFs of the propagating GPs in the dispersive medium. More specifically, a multi-target detection and localization algorithm was developed, outlined in figure 19, and detailed as follows:

(i) In order to perform a spectral decomposition, a bank of five filters, each related to a Bin-directivity, is deployed. Linear phase FIR filters are designed with a 39-tap Gaussian window, ensuring a $-29$ dB attenuation at adjacent central frequencies. Furthermore, they can be easily implemented on embedded electronic systems optimized for convolution products, maintaining low computational costs with a small number of filter taps.
It is important to note that through the filtering process, the times-of-flight (ToF) resolution is defined by a single GP rather than the duration of the excitation signal.

(ii) The undesired effect of the $k(f)$ factor in model (7) is tackled by means of appropriate weights given by $W_i = 1/K_c^2(i)$ with $i = 1, 2, \ldots, 5$. In this way, all peaks are approximately equalized according to the bin Directivity gain. The functionality of these weights will be detailed in step ($v$).

(iii) The warped frequency transform [27] is used for dispersion compensation.
The warping operator can be efficiently computed as a non-uniform FT associated with $f = Cf(k)$, followed by a conventional inverse FT [30].
Noteworthy, the non-uniform FT can be computed for the different filter outputs starting from a sample associated with the time instant $t_i$ corresponding to the initial times of actuation of the different GPs. As a result, the warped signals show GPs 'recompressed,' and those arising from

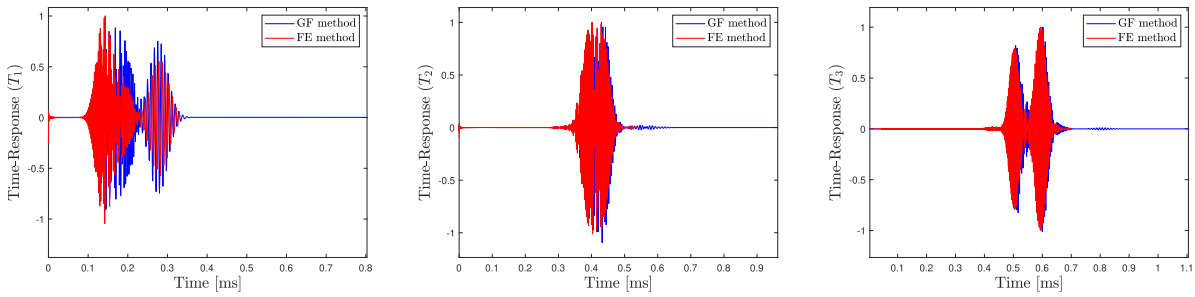


(a) DoA=33°, R=0.25 m (b) DoA=165°, R=0.45 m (c) DoA=152°, R=0.65 m

**Figure 15.** Simulated transducer (normalized) time-responses via GF and FE methods.

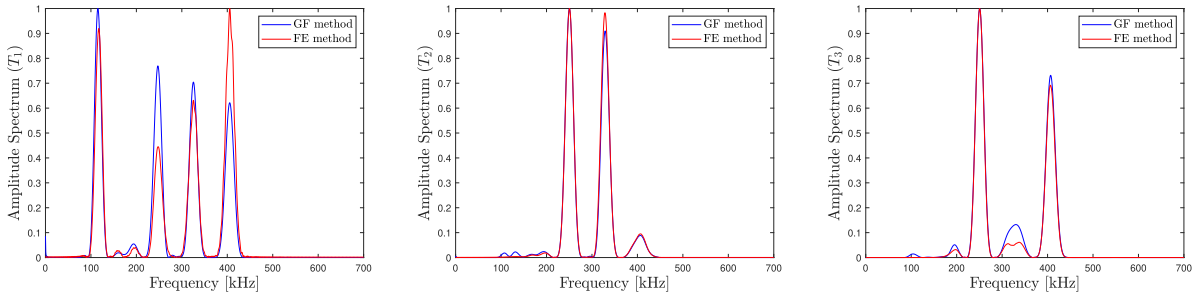


(a) DoA=33°, R=0.25 m (b) DoA=165°, R=0.45 m (c) DoA=152°, R=0.65 m

**Figure 16.** Simulated transducer (normalized) frequency-responses via GF and FE methods.

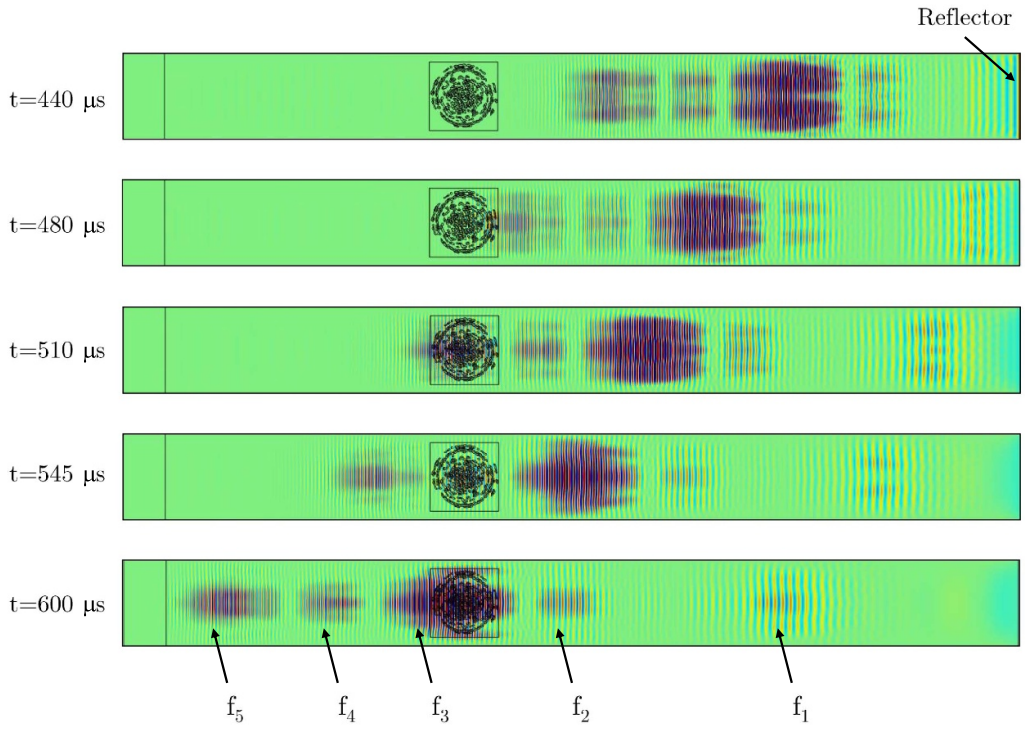


**Figure 17.** Displacement wavefield caused by the reflector at different time snapshots in scenario $T_3$. Five wave trains with different frequencies are identified as $f_1 = 106$ kHz, $f_2 = 193$ kHz, $f_3 = 249$ kHz, $f_4 = 326$ kHz, $f_5 = 407$ kHz.

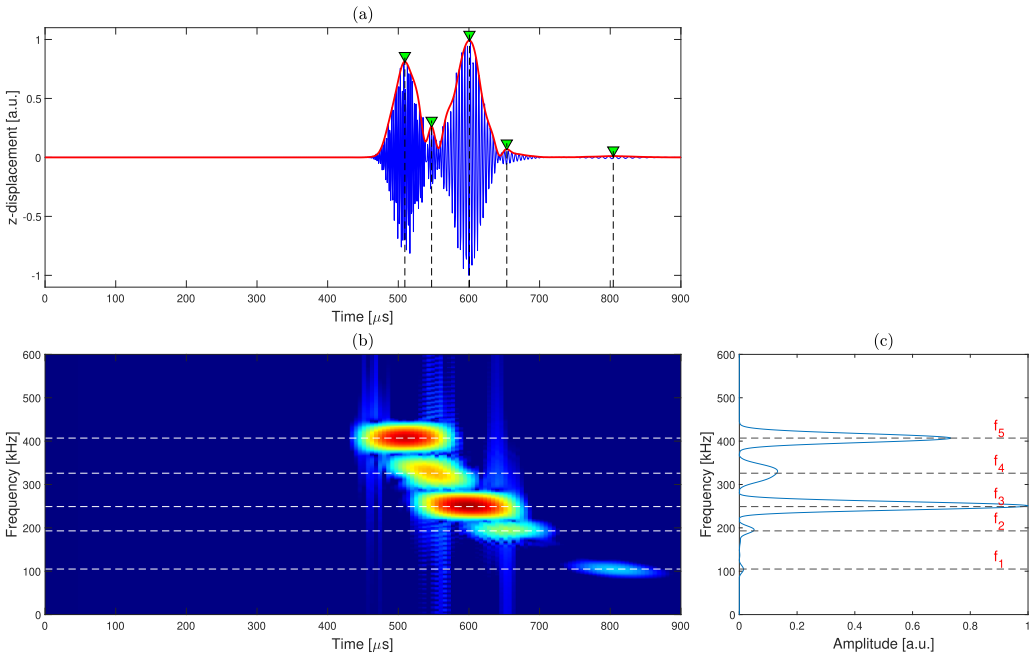


**Figure 18.** Transducer's measured response for scenario $T_3$: (a) time domain signal reflected from the damage; (b) time–frequency representation of the measured response; (c) frequency spectrum of the measured signal, where the main peak frequencies are identified as $f_1 = 106$ kHz, $f_2 = 193$ kHz, $f_3 = 249$ kHz, $f_4 = 326$ kHz, $f_5 = 407$ kHz.

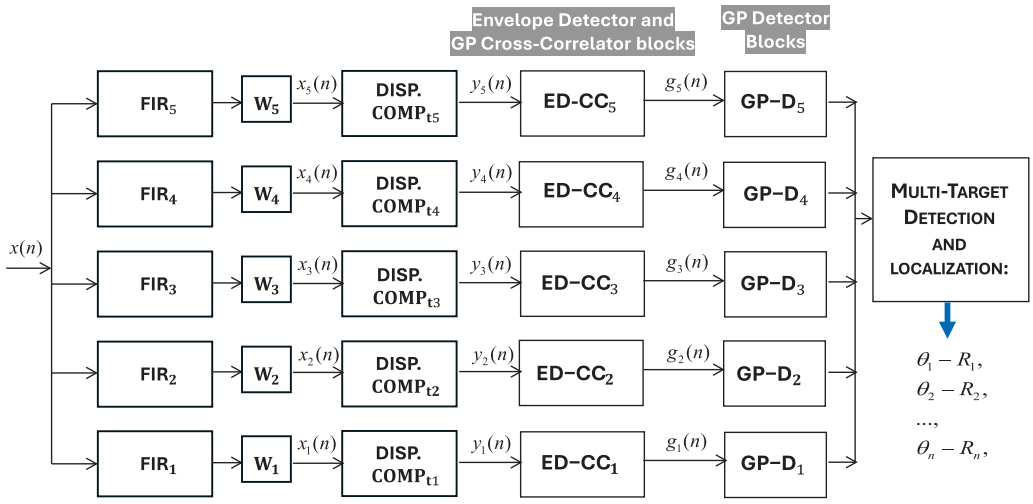


**Figure 19.** Illustrative algorithm scheme for multi-defect range angle retrieval.

the same defect are re-aligned at the same distance on the warped-time/distance axis.

(iv) The envelopes of the warped signals are computed, followed by five CC procedures with a reference-GP. These procedures provide an approximate ToF/DoF maximum likelihood (ML) estimator in the presence of additive uncorrelated Gaussian noise (AUGN) [28]).
The envelope detector can be useful when the GP phases change due to different factors (e.g. environmental changes, such as temperature fluctuations) that can slightly alter the dispersion curve $k(f)$).

(v) The Neyman–Pearson target detector [41] is considered for pulse detection and to extract the range coordinate of GPs. It defines the optimal threshold value for target detection as:

$$T_{\mathrm{N-P}} = N_{\mathrm{P}} D_{\mathrm{SNR}}\left(P_{\mathrm{fa}}\right) \tag{19}$$

where $N_{\mathrm{P}}$ is the noise power limited to the filter bands, which is supposed to be known or estimated, and $D_{\mathrm{SNR}}(\cdot)$ is the Neyman–Pearson SNR threshold detector for a desired value of false alarm rate $P_{\mathrm{fa}}$. To address the presence of sidelobes, the threshold value should be increased by the sidelobe square level $\gamma^2$, multiplied by the maximum receivable GP peak, related to the $i$th kband.

Therefore, the Detection threshold is given by:

$$T_{\text{Detect}}\left(\text{kband}_i\right) \approx \sqrt{T_{\text{N-P}}} + \gamma^2 \left(\text{kband}_i\right)_{\max_\theta} \cdot \sqrt{P_{\text{P - GP}_R}\left(\text{kband}_i\right)_{\max_\theta}}. \tag{20}$$

Observe that the weights from step (ii) can help discard false peak detection by comparing the detected peak levels.

(vi) The number of reflectors, their range, and angle coordinates are then retrieved according to the following procedure:

1. Over the five sampled output signals $g_i(n)$ in figure 19, range cells for each 'high' GPs are determined via the threshold defined in equation (20). The peak distances for each range cell are then computed, i.e. the distances associated with the maximum values within each detected range cell.
2. The total number of reflectors is determined by the number of subsets of 'high' GPs, belonging to different $k$-bands, with peak-distances varying within six times the range SD. The last one can be approximately computed (neglecting the directivity quasi-Gaussian windowing effect) via:

$$\delta R \approx \frac{v_{\text{cost}}}{\beta(\text{SNR})^{1/2}}. \tag{21}$$

where $v_{\text{const}} = 2712\,\text{m}\,\text{s}^{-1}$ (dispersion compensated A0 mode velocity) and $\beta = 2.66 B_{\text{HP}} \approx 61$ kHz. For example, considering 17 dB as SNR on the filtered signals, the SD is calculated as:

$$\text{SD} = \delta R \approx \frac{2712}{\left(61\,000 \times 50^{1/2}\right)} = 6.28\,\text{mm}. \tag{22}$$

3. The range coordinates of the reflector are estimated as the mean of halved peak distances (over a maximum of five values). Let $M$ represent the number of 'high' GPs associated with the same defect; its radial estimation accuracy (SD) is then given by:

$$\delta R \approx \frac{v_{\text{cost}}}{\sqrt{M}\beta(\text{SNR})^{1/2}}. \tag{23}$$

4. The nominal 6° angular step for each reflector is determined by comparing the subset/sequence of detected high GPs at different $k$-bands with the look-up table vectors shown in figure 3. The mean values of the previously determined steps, $\pm\delta\theta$, are then selected as the estimated angle steps for the defects, i.e. the detection equivalent mainlobe $2\delta\theta^\circ \approx 8^\circ$. Such a procedure can be applied because any estimation error between two adjacent nominal angular steps can only be attributed to the sidelobes neighbouring one of them.

### 7.2. Numerical testing

To assess the effectiveness of the designed CE-Scanning Acoustic Transducer and developed algorithms to process the recorded signal and extract multi-target range and angle information, the GF simulations of section 6.3 were used.

The scenario of three point targets of coordinates (17) in the monitored area was considered, as illustrated in figure 14.

The three distinct signals, acquired by composing the four patch signals as previously detailed in section 6.2, correspond to the three different targets resulting from two consecutive acquisition steps (according to the simulation procedure of section 6.1). These signals are illustrated in figure 20(a). Since the transducer scans all directions between 0° and 180° simultaneously, the recorded signal is represented by the sum of the three previous signals.

To consider a more realistic recorded signal, the measurement was corrupted by additive White Gaussian noise (AWGN), considering a peak SNR (PSNR) equal to 25 dB. The noise-free and noise-affected signals are illustrated in figures 20(b) and (c).

The noisy measurement is processed according to the algorithm outlined in section 7.1.

Firstly, the acquired signal $x(n)$ is given as input to the FIR filter bank. The output signals are multiplied by weights $W_i$ to compensate for the varying amplification across the different bands, as illustrated in figure 21(a).

Next, these signals are compensated for dispersion (see figure 21(b)), removing its detrimental effect on range resolution, achieving a multi-defects range accuracy of 8 cm. Noteworthy that in figure 21(b) the GPs associated with the $i$th target are located at approximately $2R_i$ distance, corresponding to a round trip from the transducer to the targets and back. As the third step, the distance-domain signal envelopes are multiplied by the distance square root function to remove the $1/\sqrt{2R}$ attenuation (7).

The signals are then cross-correlated with the reference GP envelope (figure 21(c)).

Finally, the threshold value $T_{\text{Detect}}$ (20), with $\gamma^2 = 0.32^2 \simeq 0.1$ (according to the maximum sidelobe level of beampatterns (see section 4.2)), is used to detect the GPs (figure 21(d)), avoiding false alarm detection arising from noise and sidelobe peaks. Further developments, such as the constant false alarm rate (CFAR) algorithm using [42] and sidelobe suppression techniques, can be considered for pulse detection optimization.

According to the estimation procedure (vi), the 2D damage imaging is derived, as depicted in figure 22. The number of defects along with their respective distances and angles, are estimated as follows:

$$\begin{aligned} \tilde{T}_1 &= \left(\tilde{R}_1 = 0.2513\,\text{m}\,, \tilde{\theta}_1 = 33.5^\circ\right) \\ \tilde{T}_2 &= \left(\tilde{R}_2 = 0.4531\,\text{m}\,, \tilde{\theta}_2 = 165.5^\circ\right) \\ \tilde{T}_3 &= \left(\tilde{R}_3 = 0.6497\,\text{m}\,, \tilde{\theta}_3 = 153.5^\circ\right) \end{aligned}. \tag{24}$$

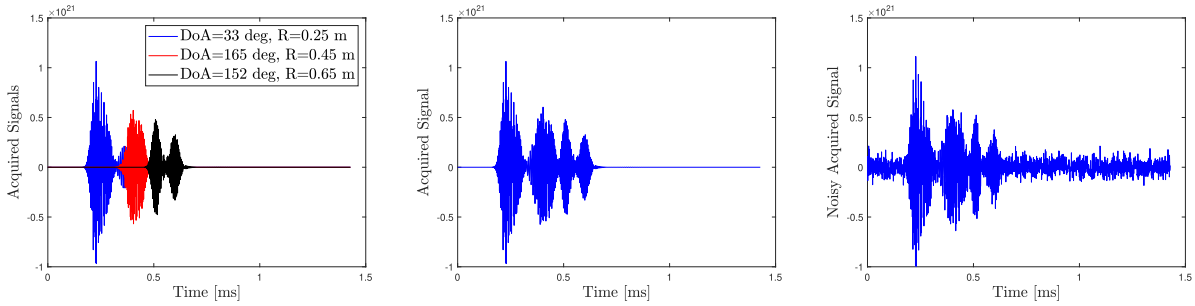


**Figure 20.** (a) Distinct detected signals due to three different targets; (b) the recorded signal as a superposition of three echoes; (c) acquired signal affected by AWGN (PSNR = 25 dB).

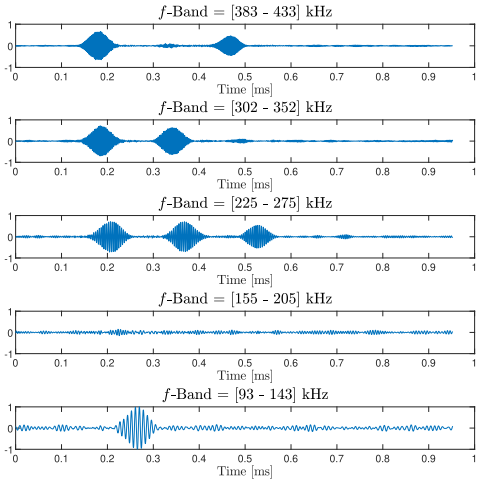


(a) FIR filtered (weighted) signals

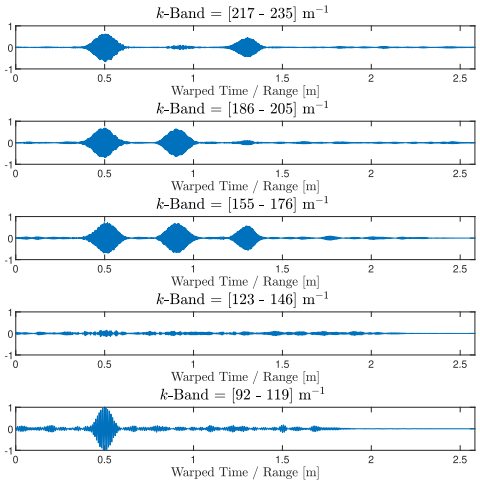


(b) Dispersion compensated signals in distance domain

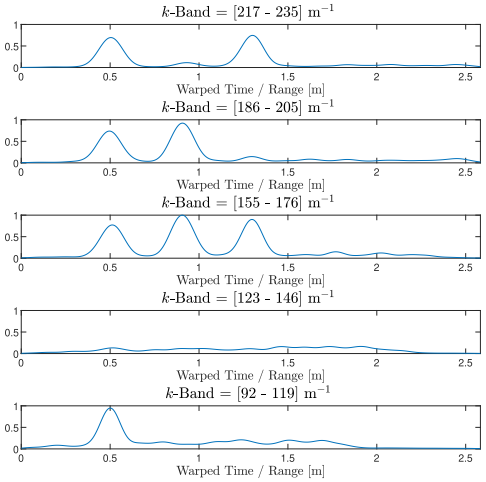


(c) Signal envelopes, cross-correlated with the envelope of a reference Gaussian Pulse

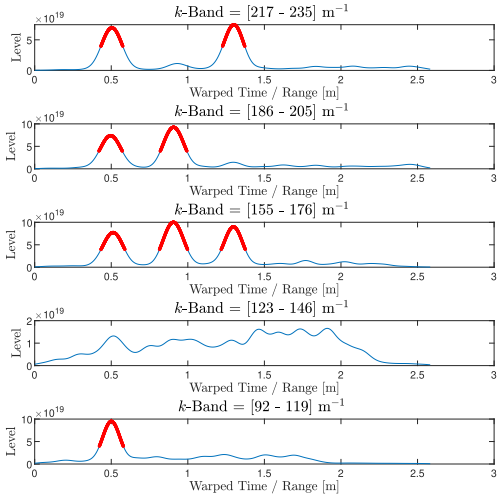


(d) GP detection via the classical Neyman-Pearson detector determines the "high" GPs and their range cell (in red color).

**Figure 21.** The output signals of each block bank of the scheme shown in figure 19, based on the recorded signal in figure 20(c).

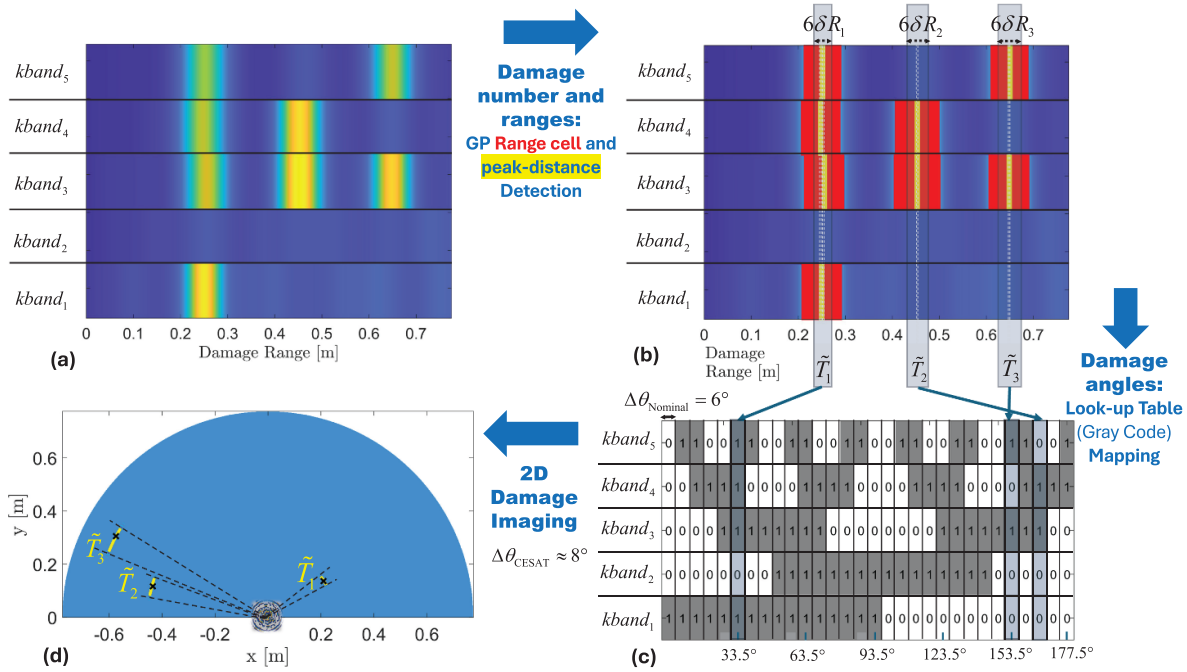


**Figure 22.** 2D damage imaging procedure: (a) five filtered, dispersion-compensated signals are cross-correlated with a reference GP; (b) GP range cells (in red) are determined according to the threshold defined by equation (20). The 'peak-distance' associated with the maximum value in each cell is identified (in yellow). The number of damage points and their ranges are estimated by multiple 'high' GPs (at different k-bands), according to the algorithm (vi); (c) the angle coordinate of each reflector is retrieved by demodulating the GP binary sequence across the five k-bands via the Gray code look-up table; (d) 2D damage imaging is obtained considering the CESAT equivalent mainlobe near to 8°, where **x** symbols indicate the actual damage positions.

The SD of DoFs, related to the three targets, computed considering the distances corresponding to the maximum values of each detected range cell (shown in red in figure 21(d)), is found to be 5.7 mm. The uncertainty in the target angle coordinates is consistently set to ≈4° (under the assumption of no false positive/negative GP detections), relative to the mean value of the estimated angle step.

It is worth mentioning that in certain engineering structures such as aircraft skins, the CESAT radial and angular resolutions, previously determined in a noisy environment, may also be adversely affected by the presence of different structural features, such as rivets, stringers, etc. To mitigate their potential adverse effects, it is necessary to minimize the typical complexity of GWs inspections [43]. To this aim, a single mode of Lamb waves, i.e. the $A_0$ mode, has been considered for ultrasonic inspections, whereas dispersion compensation procedures allow for the detection of the same waveform, regardless of the distance from the defects. Nevertheless, it should be noted that rivets, even when initially detected by the transducer, may reduce precision in determining the radial position of nearby damage. Conversely, stringers can increase the plate's absorption term [43]. This may impact the minimum detectable energy within the noise level and, consequently, the maximum range of the inspection system. More broadly, any structural features that influence either the dispersion curve or the attenuation curve may lead to reduced localization accuracy for defects or limit the maximum coverage of the transducer.

## 8. Conclusions

In this work, a single piezoelectric transducer was designed to simultaneously inspect a 2D area of plate-like structures using ultrasonic GWs, addressing the challenges of phased arrays that perform beam steering using multiple transducers. Based on the operating principle of an encoder, the proposed transducer's unique piezo-load distribution allows different binary spectral configurations to be assigned for each discrete angular step. The multi-defect range coordinates are retrieved via the DoFs of the detected peaks, while the angular information is extracted by demodulating binary sequences of peaks with approximately the same DoF across various frequencies. Therefore, the proposed piezo-transducer is referred to as CESAT. The achieved angular accuracy is approximately equal to 6°, which improves the one achieved by the previous generations of transducers (FSAT). An optimization procedure was defined to generate a feasible transducer with the desired directional properties. Numerical simulations were performed to validate the spectral encoder behavior. A signal processing scheme, based on an FIR filter Bank, dispersion compensation procedures, and peak detection of CC products, was developed for multi-reflector localization. Thanks to the low computational cost, the algorithm is suitable for embedded electronic devices. The effectiveness of the proposed transducer and the associated signal processing in damage detection and localization was assessed through both Green's Functions and FE simulations, highlighting excellent agreement. Future work aims

at improving the quantization procedures to achieve higher range resolution, developing short-circuiting techniques for the patch areas, and providing experimental results of the proposed CESAT in different practical scenarios. In the development of new generations of piezoelectric transducers, orthogonal spectral configurations will be explored, to further increase the damage imaging capability.

## Data availability statement

No new data were created or analysed in this study.

## ORCID iDs

Marco Dibiase https://orcid.org/0000-0001-7427-6761
Masoud Mohammadgholiha https://orcid.org/0000-0003-1597-6295
Luca De Marchi https://orcid.org/0000-0003-0637-9472

## References

[1] Rajagopalan J, Balasubramaniam K and Krishnamurthy C 2006 A single transmitter multi-receiver (STMR) PZT array for guided ultrasonic wave based structural health monitoring of large isotropic plate structures *Smart Mater. Struct.* **15** 1190
[2] Mitra M and Gopalakrishnan S 2016 Guided wave based structural health monitoring: a review *Smart Mater. Struct.* **25** 053001
[3] Ramalho G M F, Lopes A M and da Silva L F M 2022 Structural health monitoring of adhesive joints using Lamb waves: a review *Struct. Control Health Monit.* **29** e2849
[4] Giurgiutiu V and Cuc A 2005 Embedded non-destructive evaluation for structural health monitoring, damage detection and failure prevention *Shock Vib. Dig.* **37** 83
[5] Kessler S S, Spearing S M and Soutis C 2002 Damage detection in composite materials using Lamb wave methods *Smart Mater. Struct.* **11** 269
[6] Chen C-D, Shen Y-J, Chou P-Y and Wang P-H 2024 A Lamb-wave based SHM for multi-damage localizations in large composite plates by using piezoelectric transducer array *Smart Mater. Struct.* **33** 045028
[7] Giurgiutiu V 2003 Lamb wave generation with piezoelectric wafer active sensors for structural health monitoring *Proc. SPIE* **5056** 111–22
[8] Gorgin R, Wu Z, Gao D and Wang Y 2014 Damage size characterization algorithm for active structural health monitoring using the A0 mode of Lamb waves *Smart Mater. Struct.* **23** 035015
[9] Giurgiutiu V 2005 Tuned Lamb wave excitation and detection with piezoelectric wafer active sensors for structural health monitoring *J. Intell. Mater. Syst. Struct.* **16** 291–305
[10] Mańka M, Rosiek M, Martowicz A, Stepinski T and Uhl T 2016 PZT based tunable interdigital transducer for Lamb waves based NDT and SHM *Mech. Syst. Signal Process.* **78** 71–83
[11] Liu Z, Sun K, Song G, He C and Wu B 2016 Damage localization in aluminum plate with compact rectangular phased piezoelectric transducer array *Mech. Syst. Signal Process.* **70** 625–36
[12] Capineri L and Bulletti A 2022 Interdigitated ultrasonic transducer (Italy) *Patent* Number WO 2022/200980 A1
[13] Moetakef M A, Joshi S P and Lawrence K L 1996 Elastic wave generation by piezoceramic patches *AIAA J.* **34** 2110–7
[14] Diamanti K, Hodgkinson J and Soutis C 2002 Damage detection of composite laminates using PZT generated Lamb waves *1st European Workshop on Structural Health Monitoring* pp 398–405
[15] Wang C H, Rose J T and Chang F-K 2004 A synthetic time-reversal imaging method for structural health monitoring *Smart Mater. Struct.* **13** 415
[16] Deutsch W, Cheng A and Achenbach J 1997 Self-focusing of Rayleigh waves and Lamb waves with a linear phased array *J. Nondestruct. Eval.* **9** 81–95
[17] Giurgiutiu V and Bao J 2002 Embedded-ultrasonics structural radar for nondestructive evaluation of thin-wall structures *ASME Int. Mechanical Engineering Congress and Exposition* vol 36258 pp 333–40
[18] Lang Y-F, Tian S-H, Yang Z-B, Zhang W, Kong D-T, Xu K-L and Chen X-F 2021 Focusing phase imaging for Lamb wave phased array *Smart Mater. Struct.* **31** 025001
[19] Yu L and Giurgiutiu V 2008 *In situ* 2-D piezoelectric wafer active sensors arrays for guided wave damage detection *Ultrasonics* **48** 117–34
[20] Grigg S, Pullin R, Pearson M, Jenman D, Cooper R, Parkins A and Featherston C A 2021 Development of a low-power wireless acoustic emission sensor node for aerospace applications *Struct. Control Health Monit.* **28** e2701
[21] Kudela P, Radzienski M, Miniaci M, Fiborek P and Ostachowicz W 2024 An ultrasensitive device with embedded phononic crystals for the detection and localisation of nonlinear guided waves (arXiv:2406.17370)
[22] Du Y and Miao H 2024 A radar transducer for unidirectionally emitting and steering SH guided wave *Ultrasonics* **143** 107414
[23] Senesi M and Ruzzene M 2011 A frequency selective acoustic transducer for directional Lamb wave sensing *J. Acoust. Soc. Am.* **130** 1899–907
[24] De Marchi L, Mohammadgholiha M and Dibiase M 2023 Frequency steerable transducers for ultrasonic structural health monitoring *2023 IEEE Int. Ultrasonics Symp. (IUS)* (IEEE) pp 1–8
[25] Dibiase M, Mohammadgholiha M and De Marchi L 2022 Optimal array design and directive sensors for guided waves DoA estimation *Sensors* **22** 780
[26] Mohammadgholiha M, Moll J and De Marchi L 2023 A new generation of piezoceramic frequency steerable acoustic transducers for the rapid inspection of large areas of metallic plate structures *2023 IEEE Int. Ultrasonics Symp. (IUS)* (IEEE) pp 1–4
[27] De Marchi L, Perelli A and Marzani A 2013 A signal processing approach to exploit chirp excitation in Lamb wave defect detection and localization procedures *Mech. Syst. Signal Process.* **39** 20–31
[28] van Der Heijden F, Duin R P, De Ridder D and Tax D M 2005 *Classification, Parameter Estimation and State Estimation: An Engineering Approach Using MATLAB* (Wiley)
[29] Yang J 2006 Three-Dimensional Theories *Mechanics of piezoelectric structures* (World Scientific) pp 1–22
[30] Baravelli E, Senesi M, Ruzzene M, De Marchi L and Speciale N 2011 Double-channel, frequency-steered acoustic transducer with 2-D imaging capabilities *IEEE Trans. Ultrason. Ferroelectr. Freq. Control* **58** 1430–41
[31] Simonetti F 2006 Multiple scattering: the key to unravel the subwavelength world from the far-field pattern of a scattered wave *Phys. Rev.* E **73** 036619
[32] Skolnik M 2001 *Introduction to Radar Systems* (*Electrical Engineering Series*) (McGraw-Hill)
[33] Reyes O A M, Zima B, Moll J, Mohammadgholiha M and de Marchi L 2022 A numerical study on baseline-free damage detection using frequency steerable acoustic transducers *European Workshop on Structural Health Monitoring* (Springer) pp 24–33

[34] Sadia H, Sherien S, Iqbal H, Zeeshan M, Khan A and Rehman S 2017 Range estimation in radar using maximum likelihood estimator *2017 20th Int. Conf. Computer and Information Technology (ICCIT)* (IEEE) pp 1–5

[35] Perelli A, De Marchi L, Marzani A and Speciale N 2012 Acoustic emission localization in plates with dispersion and reverberations using sparse PZT sensors in passive mode *Smart Mater. Struct.* **21** 025010

[36] Hahn W and Tretter S 1973 Optimum processing for delay-vector estimation in passive signal arrays *IEEE Trans. Inf. Theory* **19** 608–14

[37] Knuth D 2014 *The Art of Computer Programming, Volume 4A: Combinatorial Algorithms, Part 1* Part 1 (Pearson Education)

[38] COMSOL AB 2020 COMSOL multiphysics v. 5.6. (available at: www.comsol.com)

[39] Mohammadgholiha M, Zonzini F, Moll J and De Marchi L 2023 Directional multi-frequency guided waves communications using discrete frequency-steerable acoustic transducers *IEEE Trans. Ultrason. Ferroelectr. Freq. Control* **70** 1494–505

[40] Mei H and Giurgiutiu V 2018 Effect of structural damping on the tuning between piezoelectric wafer active sensors and lamb waves *J. Intell. Mater. Syst. Struct.* **29** 2177–91

[41] Kay S 1998 *Fundamentals of Statistical Signal Processing: Detection Theory* (*Fundamentals of Statistical Si*) (Prentice-Hall PTR)

[42] Machado-Fernández J R, Mojena-Hernandez N and Bacallao-Vidal J C 2017 Evaluation of CFAR detectors performance *Iteckne* **14** 170–8

[43] Ricci F, Monaco E, Maio L, Boffa N D and Mal A K 2016 Guided waves in a stiffened composite laminate with a delamination *Struct. Health Monit.* **15** 351–8